energies

MDPI

Article

Rigid-Flexible Modal Analysis of the Hydraulic 6-DOF Parallel Mechanism

Chenyang Zhang * and Hongzhou Jiang

School of Mechatronics Engineering, Harbin Institute of Technology, West Dazhi Street No. 92, Harbin 150000, China; jianghz@hit.edu.cn

* Correspondence: zhangchenyang@hit.edu.cn; Tel.: +86-132-6368-9929

Abstract: In view of the problems encountered in previous hydraulic 6-DOF parallel mechanism projects, flexible modes appear that the actual natural frequencies of x and y degrees of freedom of the parallel mechanism are lower than those obtained through calculation. The phenomenon above not only decreases the dynamic response characteristics of the mechanism, but also leads to doubts about the actual performance of the mechanism. The real reason for the phenomenon above is solved in this paper. First the flexible structure of the hydraulic cylinder is analyzed and simplified, and then the dynamic model of the rigid-flexible 6-DOF parallel mechanism is established with the extended Hamilton's principle. Finally the rigid-flexible modes are calculated with the dynamic model obtained, further analysis and verification with a simulation model and an experimental platform are also conducted. Results show that the phenomenon of the flexible modes is mainly caused by the O-rings of the step-seals of the guide sleeve and those with less elasticity should be adopted to keep the dynamic characteristics of the parallel mechanism.

Keywords: rigid-flexible; modal analysis; 6-DOF parallel mechanism; dynamic model; extended Hamilton's principle

Citation: Zhang, C.; Jiang, H. Rigid-Flexible Modal Analysis of the Hydraulic 6-DOF Parallel Mechanism. *Energies* **2021**, *14*, 1604. https://doi.org/10.3390/en14061604

Academic Editor: João Carlos de Campos Henriques

Received: 14 January 2021
Accepted: 5 March 2021
Published: 13 March 2021

1. Introduction

In recent years, many studies have focused on the parallel mechanisms due to the advantages such as high payload to weight ratio, high structural rigidity and high dynamic capabilities [1–4]. With the rapid development of the parallel mechanisms in the direction of heavy load, high speed and light weight, many parallel mechanisms that were previously considered to be rigid have become flexible, and more and more attention is being paid to the dynamic characteristics and the control methods of rigid-flexible parallel mechanisms. The dynamic equations of a 3-TPT parallel manipulator with flexible links were derived analytically based on the Newton's second law and the Lagrange multiplier approach by Zhu et al. [5]. Gu et al. analysed the kinematic model of a novel continuum robot with an optimized flexible parallel mechanism for transoral robotic surgery (TORS) [6]. Liu et al. explored the dynamics of a spatial parallel manipulator with rigid and flexible links with the finite element method [7]. Chen et al. established the nonlinear elastic dynamic model of a 4-UPS-UPU flexible parallel mechanism under the ideal situation based on the finite element method. A methodology to precisely control the motion of a 4-DOF hybrid parallel-serial rigid-flexible micro-mechanism with haptic feedback control strategy was developed by Pinskier et al. [8]. Firoozabadi et al. established the dynamic model of a 3-RPR planar parallel manipulator with three flexible intermediate links which were modeled as Euler-Bernoulli beams with two types of the fixed-pinned and the fixed-free boundary conditions based on the assumed mode method [9]. Wu et al. investigated the mechatronics model and forced vibration of a 2-DOF parallel manipulator in a 5-DOF hybrid machine tool by using bond graphs, where the elastic deformation of the link with the lowest stiffness was considered in the modeling [10]. Wang et al. analyzed the natural frequencies of a 3SPS+1PS parallel hip joint manipulator based on the rigid finite element

method and the flexible finite element method [11]. While the flexibility of the parallel mechanisms in the above literatures is obvious and set in advance, it is of great engineering significance to identify the reason for the flexibility existing in a parallel mechanism which was considered as rigid.

The hydraulic 6-DOF parallel mechanism is widely used in fields of flight training and motion simulation [12–16]. The upper limit of its dynamic characteristics is mainly determined by its natural frequencies of x and y degrees of freedom which are basically the same due to the symmetry of the mechanism and are the smallest in value among the total six rigid modes [17]. While in the previous hydraulic 6-DOF parallel mechanism projects, flexible modes appear that the actual natural frequencies of x and y degrees of freedom of the hydraulic 6-DOF parallel mechanism are lower than those obtained through calculation, which not only decreases the dynamic response characteristics of the mechanism, but also leads to a doubt about its actual performances. The phenomenon above can be observed from the bode diagram of the experimental 6-DOF parallel mechanism while further analysis is not conducted [18]. The structural flexibility of the hydraulic cylinder which is the main part of the parallel mechanism is studied, while further analysis has not been conducted due to the complex structure of the parallel mechanism [19,20]. The flexible modal phenomenon which the actual modal frequency is about 11.3 Hz compared with about 17 Hz through calculation is described and the transverse vibration of the hydraulic cylinder is roughly considered as the main reason by Li, but the above conclusion is only based on the equations of the transverse vibration of the hydraulic cylinder instead of the whole parallel mechanism [21]. So a complete 6-DOF parallel mechanism dynamic model considering the flexibility of the hydraulic cylinder should be established with verification of simulation and experiment to find the real reason of the flexible modes, which is conducted in this paper.

2. Introduction to the 6-DOF Parallel Mechanism

Figure 1 shows a schematic of the 6-DOF parallel mechanism. In this mechanism, the spatial motion of the moving platform is generated by six hydraulic legs. Each hydraulic leg consists of two parts connected with a gimbal joint. The mechanism has a total of six degrees of freedom, including three degrees of freedom of translation (x,y,z) and three degrees of freedom of rotation around the axis (rx,ry,rz).

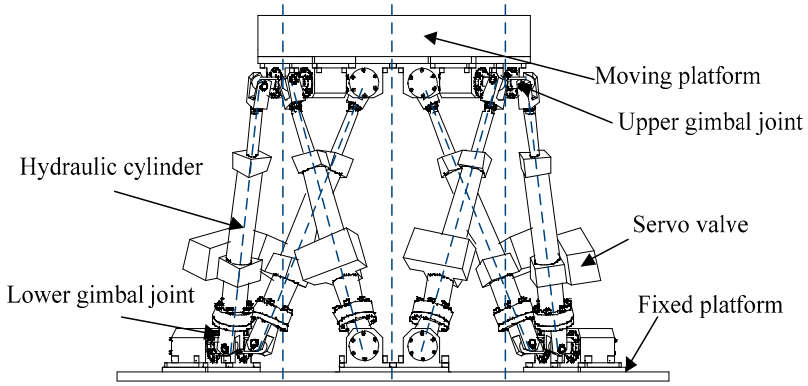

Figure 1. Schematic diagram of the 6-DOF parallel mechanism.

3. Dynamic Model of the Rigid-Flexible 6-DOF Parallel Mechanism

Since components mounted on the cylinder case and the piston rod can be treated like part of them, the dynamics of the components mounted on the cylinder case as well as the piston rod can be reasonably ignored. Thus the hydraulic leg of the parallel mechanism can still be divided into a cylinder case and a piston rod. Ignoring the accessories, the structure of the hydraulic cylinder is shown in Figure 2.

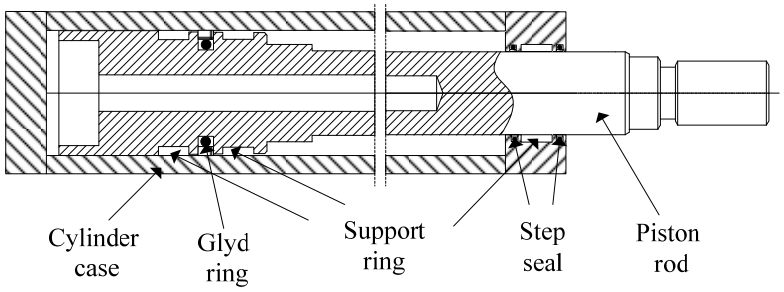

Figure 2. Structure diagram of the hydraulic cylinder.

Generally, the piston rod and the cylinder case can be considered as rigid. Since the O-rings of the glyd-ring and the step-seals provide the sealing pressure for the piston and the guide sleeve, and the elastic moduluses of them are quite small compared with those of the piston rod and the cylinder case, it can be considered that the O-rings in the glyd-ring and the step-seals are the flexible part and the root cause of the flexible modes, and a dynamic model of the 6-DOF parallel mechanism considering the flexibility of the O-rings should be established for further study.

Usually, the O-rings of the step-seals are prone to damage based on practical experience, and the elasticity of the O-ring of the glyd-ring is smaller than that of the step-seals in practice. In order to facilitate the modeling, the flexibility of the glyd-ring is ignored. Due to the double gimbal structure of the mechanism, it is difficult to find the generalized coordinates to describe the flexible deformation. Referring to the derivation of the viscous matrix of the rigid 6-DOF parallel mechanism in [22], two axes which are perpendicular and independent to each other are applied. These two axes which are parallel to the axes of the lower gimbal joint are called the flexible axes and two revolute joints are imported to describe the motion of the piston rod around the flexible axes. These two axes are located at the piston for convenience. Since the structure and parameters of the two revolute joints are the same, only one of them is described which is shown in Figure 3.

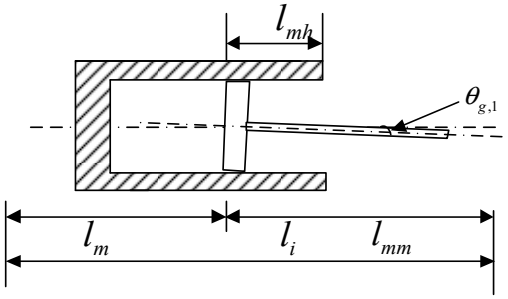

Figure 3. Structure diagram of the flexible deformation.

In Figure 3, l_i is the length of a single hydraulic leg, l_m and l_{mn} are the length from the piston to the lower gimbal joint and the length from the piston to the upper gimbal joint, l_{mh} is the length from the guide sleeve to the piston, $\theta_{g,1}$ is the rotation angle of the piston rod around the flexible axis 1. The schematic diagram of the i-th leg and the moving platform is shown in Figure 4, where a_i^p is the position of the upper gimbal joint with respect to O_p, f_i is the constraint force applied by the upper gimbal joint, F_{ai} is the actuation force exerted by the piston rod. The extended Hamilton's principle should be adopted to establish the dynamic model [23].

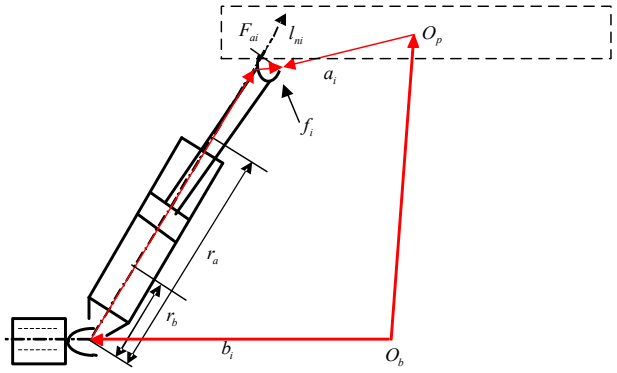

Figure 4. The schematic diagram of the i-th leg and the moving platform.

Actually the phenomenon of flexible modes can be observed in parallel mechanisms with smooth joints and regular joints, so the friction of the joints and the gravity load are ignored in the modeling process, and due to the symmetry of the 6-DOF parallel mechanism, only one of the six hydraulic legs is needed to develop the equations of motion. According to the above description, the kinetic energy of the *i*-th leg is:

$$T_i = T_t + T_g + T_\omega, \tag{1}$$

where $T_t = \frac{1}{2}m_t\left(\dot{\theta}_i \times r_b\right)^2$ is the kinetic energy of the cylinder case, $T_g = \frac{1}{2}m_g\left(\dot{\theta}_i \times r_a + \dot{l}_i + \dot{\theta}_{g,1,i} \times (r_a - l_m) + \dot{\theta}_{g,2,i} \times (r_a - l_m)\right)^2$ is the kinetic energy of the piston rod, $T_\omega = \frac{1}{2}i_t\theta_i^2 + \frac{1}{2}i_r\left(\dot{\theta}_i + \dot{\theta}_{g,1,i} + \dot{\theta}_{g,2,i}\right)^2$ is the rotational kinetic energy of the cylinder case and the piston rod, m_t is the mass of the cylinder case, m_g is the mass of the piston rod, r_b is the mass center position of the cylinder case relative to the lower gimbal joint, r_a is the mass center position of the piston rod relative to the lower gimbal joint, l_m is the piston position relative to the lower gimbal joint, i_t is the moment of inertia of the cylinder case, i_r is the moment of inertia of the piston rod, $\dot{\theta}_i$ is the angular velocity of the cylinder case around the lower gimbal joint, $\dot{\theta}_{g,2,i}$ and $\dot{\theta}_{g,1,i}$ are the angular velocities of the piston rod around the flexible axis 2 and the flexible axis 1. The potential energy of the i-th leg can be expressed as:

$$V_i = \frac{1}{2}k\left[\left(\theta_{g,1,i} \times l_{mh}\right)^2 + \left(\theta_{g,2,i} \times l_{mh}\right)^2\right], \tag{2}$$

where k is the equivalent spring coefficient of the guide sleeve, l_{mh} is the guide sleeve position relative to the piston. The virtual work of the *i*-th leg can be written as:

$$\delta W = f_i \cdot \delta r_{Ci} + F_{ai} \cdot \delta l_i, \tag{3}$$

where f_i is the constraint force applied by the upper gimbal joint, $f_i = \begin{bmatrix} f_{ix} & f_{iy} & f_{iz} \end{bmatrix}^T$, F_a is the actuation force exerted by the piston rod, δr_C is the virtual displacement of the upper gimbal joint, δl_i is the virtual displacement of the piston rod. The differential equations are developed by the extended Hamilton's principle, which is presented as:

$$\int_{t_1}^{t_2} (\delta T - \delta V + \delta W)dt = 0, \tag{4}$$

Evaluating the variation of Equations (1)–(3), substituting the results into Equation (4), and integrating by parts leads to the equations of motion expressed as:

$$\begin{aligned}\left[m_t|r_b|^2\widetilde{l}_{ni}{}^T\widetilde{l}_{ni}+m_g|r_a|^2\widetilde{l}_{ni}{}^T\widetilde{l}_{ni}+i_r+i_t\right]\ddot{\theta}_i+\left[m_g|r_a(r_a-l_m)|\widetilde{l}_{ni}{}^T\widetilde{l}_{ni}\theta_{g,1,ni}+i_r\theta_{g,1,ni}\right]\ddot{\theta}_{g,1,i}\\+\left[m_g|r_a(r_a-l_m)|\widetilde{l}_{ni}{}^T\widetilde{l}_{ni}\theta_{g,2,ni}+i_r\theta_{g,2,ni}\right]\ddot{\theta}_{g,2,i}=\widetilde{l}_i\begin{bmatrix} f_{ix} & f_{iy} & f_{iz}\end{bmatrix}^T\end{aligned}, \tag{5}$$

$$m_t\dot{l}_i+m_g\dot{l}_i=f_{ai}+l_{ni}^T\begin{bmatrix} f_{ix} & f_{iy} & f_{iz}\end{bmatrix}^T, \tag{6}$$

$$\begin{aligned}\left(m_g|(r_a-l_m)r_a|\theta_{g,2,ni}^T\widetilde{l}_{ni}^T\widetilde{l}_{ni}+\theta_{g,2,ni}^Ti_r\right)\ddot{\theta}_i\\+\left[m_g|r_a-l_m|^2\theta_{g,2,ni}^T\widetilde{l}_{ni}^T\widetilde{l}_{ni}\theta_{g,2,ni}+i_r\right]\ddot{\theta}_{g,2,i}=\theta_{g,2,ni}^T\widetilde{l}_{mh}\begin{bmatrix} f_{ix} & f_{iy} & f_{iz}\end{bmatrix}^T\end{aligned}, \tag{7}$$

$$\begin{aligned}\left(m_g|(r_a-l_m)r_a|\theta_{g,1,ni}^T\widetilde{l}_{ni}^T\widetilde{l}_{ni}+\theta_{g,1,ni}^Ti_r\right)\ddot{\theta}_i\\+\left[m_g|r_a-l_m|^2\theta_{g,1,ni}^T\widetilde{l}_{ni}^T\widetilde{l}_{ni}\theta_{g,1,ni}+i_r\right]\ddot{\theta}_{g,1,i}=\theta_{g,1,ni}^T\widetilde{l}_{mh}\begin{bmatrix} f_{ix} & f_{iy} & f_{iz}\end{bmatrix}^T\end{aligned}, \tag{8}$$

where $\widetilde{l}_{ni}$ and $\widetilde{l}_{ni}{}^T$ are the anti-symmetric matrix and its transpose matrix generated from the vector l_{ni}, $\widetilde{l}_i$ is the anti-symmetric matrix of the vector l_i, l_{ni}^T is the transpose matrix of the vector l_{ni}, l_{ni} is the 3×1 unit vector of the vector l_i, l_i is the 3×1 vector between the two gimbal points of the hydraulic leg, $\theta_{g,1,ni}$ and $\theta_{g,1,ni}^T$ are the 3×1 unit vector and its transpose vector of the flexible axis 1, $\theta_{g,2,ni}$ and $\theta_{g,2,ni}^T$ are the 3×1 unit vector and its transpose vector of the flexible axis 2, $\widetilde{l}_{mh}$ is the anti-symmetric matrix from the vector l_{mh}. The moving platform of the mechanism is still considered to be rigid. The dynamic model of the moving platform is obtained by means of Newton's second law as:

$$M_p\ddot{q}=-J_{l,q}^Tf_i, \tag{9}$$

where $J_{l,q}^T$ is the transpose matrix of the vector $J_{l,q}$, $J_{l,q}$ is the jacobin matrix between the work space and the hydraulic legs. According to Figure 4, the speed constraint equation of the 6-DOF parallel mechanism can be written as:

$$\dot{l}_i+\dot{\theta}_i\times l_i+\dot{\theta}_{g,1,i}\widetilde{\theta}_{g,1,ni}l_{mm}+\dot{\theta}_{g,2,i}\widetilde{\theta}_{g,2,ni}l_{mm}=\dot{c}+\dot{R}\times a^p \tag{10}$$

For convenience, the displacement of the hydraulic cylinder and the rotation angle of the piston rod around flexible axes are selected as the generalized coordinates. Referring to Equation (10), the angular velocity of the cylinder case around the lower gimbal point can be written as:

$$\dot{\theta}_i=J_{ai,q}\left[\dot{q}\right]-J_{\theta_i,\theta_{g1}}\left[\dot{\theta}_{g,1}\right]-J_{\theta_i,\theta_{g2}}\left[\dot{\theta}_{g,2}\right], \tag{11}$$

where: $J_{ai,q}=\begin{bmatrix}\frac{1}{|l_i|}\widetilde{l}_{ni} & \frac{1}{|l_i|}\widetilde{l}_{ni}\left(a_i^p\right)\end{bmatrix}$, $J_{\theta_i,\theta_{g1}}=\frac{|l_{mm}|}{|l_i|}diag\left[\theta_{g,1,ni}\right], i=1\sim6$, $J_{\theta_i,\theta_{g2}}=\frac{|l_{mm}|}{|l_i|}diag\left[\theta_{g,2,ni}\right], i=1\sim6$.

Since the deformation at the upper gimbal joint caused by the O-rings of the guide sleeve is perpendicular to the moving direction of the piston rod. The jacobi matrix $J_{l,q}$ are the same in the rigid model and the rigid-flexible model as:

$$\dot{l}=J_{l,q}\dot{q}, \tag{12}$$

where q is the six generalized vectors of the moving platform. Substituting Equation (12) into Equation (11), the relationship between the angular velocities of the cylinder cases around the lower gimbal joints and the velocities of the generalized coordinates can be written as:

$$\dot{\theta}_i=J_{ai,l}\left[\dot{q}\right]-J_{\theta_i,\theta_{g1}}\left[\dot{\theta}_{g1}\right]-J_{\theta_i,\theta_{g2}}\left[\dot{\theta}_{g2}\right], \tag{13}$$

where $J_{ai,l} = J_{ai,q}J_{l,q}^{-1}$. The coriolis force and the centripetal force can be omitted for the small range motion. Differentiating Equation (13) with respect to time gives:

$$\ddot{\theta}_i = J_{ai,l}\left[\ddot{q}\right] - J_{\theta_i,\theta_{g1}}\left[\ddot{\theta}_{g1}\right] - J_{\theta_i,\theta_{g2}}\left[\ddot{\theta}_{g2}\right], \tag{14}$$

similarly, derivation can be performed on both sides of Equation (12), so the relationship between the accelerations of the piston rods and the accelerations of the moving platform can be obtained as:

$$\ddot{l} \approx J_{l,q}\ddot{q}, \tag{15}$$

referring to [23], substituting Equation (14) and Equation (15) into Equations (5)–(9), and as constraint force does not do any work, the dynamic model of the rigid-flexible 6-DOF parallel mechanism can be obtained. For the rigid 6-DOF parallel mechanism, the modeling process is quite similar, ignoring the above flexible deformation, the dynamic equations of the rigid 6-DOF parallel mechanism can be easily obtained, which is the same in value with those deduced with Kane's method in [22]. It is worth nothing that the inertia parameter matrix of the dynamic model of the rigid model is the same as the 6×6 matrix located upper-left of the inertia matrix of the rigid-flexible model.

4. Simulation Model and Model Verification

The dynamic model obtained above is verified by comparing the modes of the dynamic model and a simulation model. The hydraulic cylinder brings out hydraulic spring stiffness, which can be calculated as:

$$k_h = \beta_e \frac{\left(1 + e^2\right) A_p^2}{V_0}, \tag{16}$$

where β_e is the oil bulk modulus, e is the area ratio of the rod cavity to the rod-less cavity, A_p is the piston area, V_0 is the control volume of the cylinder. Combined with the elastic matrix caused by the O-rings of the guide sleeve, the complete elastic matrix of the parallel mechanism is obtained. Modal parameters can be obtained by solving eigenfunction of:

$$\left(-\omega^2 M + K\right)\varphi = 0, \tag{17}$$

which provides the modal frequencies ω and the modes φ. It is worth noting that, for the rigid-flexible 6-DOF parallel mechanism, 18 modes can be obtained with Equation (17), while only six modes can be obtained with the rigid dynamic model. A simulation model is set, two revolute joints with torque spring are added in the cylinder model to imitate the effect of the O-rings of the guide sleeve, which are shown in Figure 5.

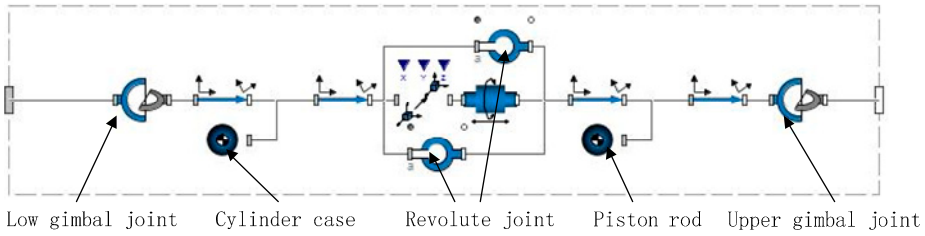

Figure 5. Schematic diagram of the cylinder model in the simulation model.

The configuration parameters and the dynamic parameters of the simulation model are shown in Table 1.

Table 1. Configuration parameters and dynamic parameters of the simulation model.

Descriptions	Value
Distribution radius of upper joint points (m)	0.5995
Distribution radius of lower joint points (m)	0.4
Platform height in neutral position (m)	0.783
Lower gimbal spacing (m)	0.17
Upper gimbal spacing (m)	0.17
The length of the hydraulic actuator (m)	0.86
Height of the moving platform mass center (m)	0.163
Mass of the moving platform (kg)	894
Spring stiffness coefficient of the equivalent spring (N/m)	1.5732×10^5
Oil bulk modulus (MPa)	700

By substituting the parameters in Table 1 into the simulation model, bode diagram of the rigid-flexible simulation model can be obtained, which is shown in Figure 6.

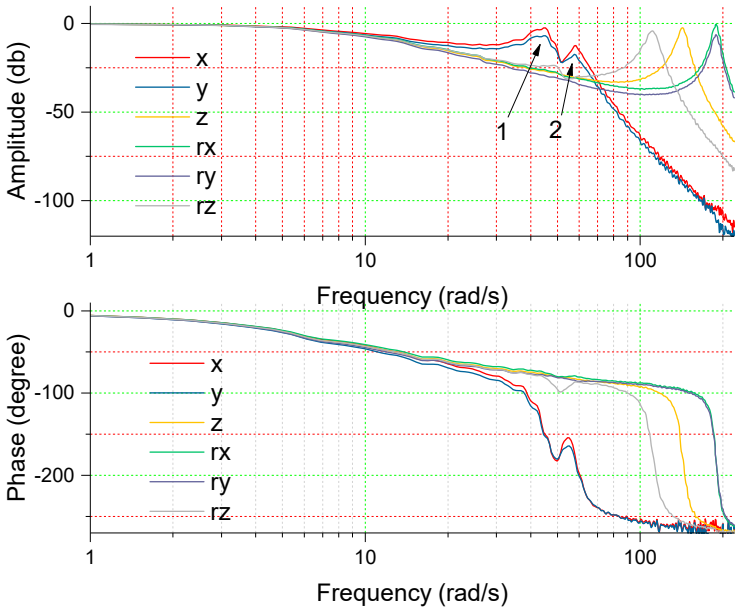

Figure 6. Bode diagram of the rigid-flexible simulation model.

From Figure 6, it is found that two modes named mode 1 and mode 2 appear in x and y degrees of freedom, while only one mode can be found in other degrees of freedom and by substituting the parameters in Table 1 into Equation (17), the modal frequencies of the rigid-flexible dynamic model can be obtained and are shown in Table 2.

Table 2. Modal frequencies of the rigid-flexible dynamic model.

No.	Frequency (Rad/s)	No.	Frequency (Rad/s)	No.	Frequency (Rad/s)
1	189.32	7	53.39	13	53.35
2	189.32	8	53.39	14	53.35
3	143.38	9	53.39	15	53.30
4	112.21	10	53.39	16	53.30
5	53.5	11	53.39	17	46.78
6	53.39	12	53.35	18	46.78

From Table 2, it can be seen that 18 modes can be obtained from the dynamic model, while only 8 modal frequencies can be found from Figure 6. However, this situation is due

to the correlation between the rigid motion and the flexible motion, and since the modal frequencies with Equation (17) of the rigid-flexible dynamic model are basically the same with the modal frequencies from Figure 6, the simulation model and the dynamic model of the rigid-flexible 6-DOF parallel mechanism both share high accuracy. By increasing the spring stiffness coefficient of the simulation model, the effects of the O-rings of the step-seals on the modes can be eliminated, the rigid-flexible simulation model turns into a rigid simulation model again, bode diagram of the rigid simulation model is shown in Figure 7.

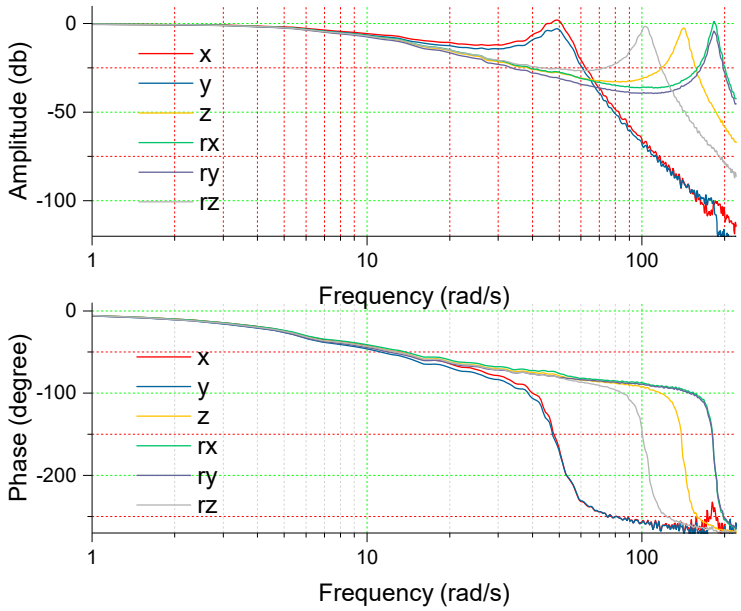

Figure 7. Bode diagram of the rigid simulation model.

From Figure 7, it can be found that only one mode can be found in the bode diagram of x or y degree of freedom, and since the modal frequencies of x and y degrees of freedom in Figure 7 are bigger than those of mode 1 in Figure 6, the elasticity of the O-rings of the step-seals is the main reason for flexible modals, while no obvious effects are found in bode diagram of other degrees of freedom. It also should be noted that the modal frequencies of the rigid simulation model in Figure 7 are basically the same with those of the dynamic model calculated with Equation (17).

5. Experimental Verification

Experiments are also conducted to verify the results obtained above on an experimental platform. The structure parameters of the experimental platform are basically the same with the simulation model, but the inertia load is different. Both step-seals and glyd-rings are adopted in the cylinders of the experimental platform, the structure of the experimental platform is shown in Figure 8.

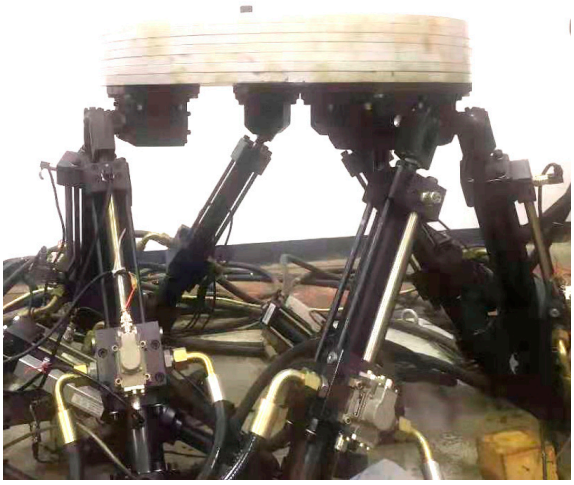

Figure 8. Structure diagram of the experimental platform.

A real-time control system is used to control the experimental platform and to record the data. The position and pose of the experimental platform are calculated with the leg lengths which are acquired with a data sample card and the drive currents of the servo valves are obtained with the position and pose errors and a signal-conditioning module. The experimental process is illustrated as follows. First, move the moving platform to the middle position, then the complete bode diagram of the experimental platform can be obtained by exciting in all 6-DOF with white noise signals and Fourier transform next, which is shown in Figure 9.

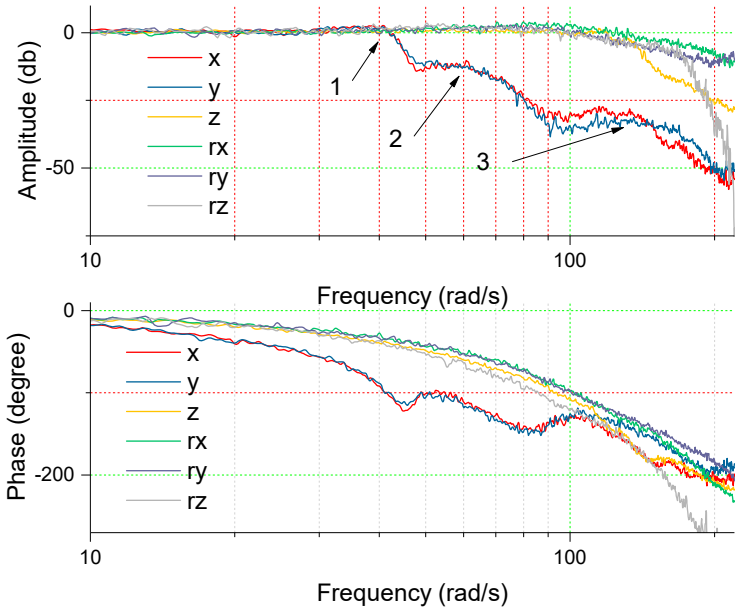

Figure 9. Bode diagram of the experimental platform.

From Figure 9, it is found that the Bode diagram of the experimental platform is quite similar to that of the simulation model in general, flexible modes also appear that three modes named mode 1, mode 2 and mode 3 can be observed in both x and y degrees of freedom, while only one mode can be found in other degrees of freedom. Since the modal frequency of mode 3 is far from those of mode 1 and mode 2 in the Bode diagram and is cause by the O-ring of the glyd-ring, The Bode diagram of only mode 1 and mode 2 should be considered. The modal frequencies of mode 1 and mode 2 are a little different with those of Figure 6 which is due to the differences of the inertial parameters and the structural

parameters between the simulation model and the experimental platform, the wave forms are quite similar, and it can be clearly confirmed that the flexible modes are main caused by the O-rings of the step-seals of the guide sleeve, while no obvious effects are found in Bode diagram of other degrees of freedom of the experimental platform, which is also in agree with the simulation model. Though the structural parameters and the inertial parameters of the experimental platform in this paper and the parallel mechanism in [19] are quite different, the waveforms of the Bode diagrams are quite similar which also supports the analysis above. By comparing Bode diagrams of Figures 6, 7 and 9, it can be concluded that the flexible modes in Figure 9 will disappear and the rigid-flexible 6-DOF parallel mechanism will become rigid again by replacing the O-rings of the step-seals of the guide sleeve with those of less elasticity, which is of great engineering significance to eliminate its influences on the dynamic characteristics of the hydraulic 6-DOF parallel mechanism.

6. Conclusions

The real reason for the phenomenon in the previous hydraulic 6-DOF parallel mechanism projects that the actual natural frequencies of x and y degrees of freedom are lower than those obtained through calculation is solved by the combination of the complete dynamic model considering the flexibility of the hydraulic cylinder and verifications with a simulation model and an experimental platform in this paper. The conclusions are organized as follows: The phenomenon of the flexible modes of the hydraulic 6-DOF parallel mechanism is mainly caused by the O-rings of the step-seals of the guide sleeve, which basically do not have any influences on the dynamic characteristics of other degrees of freedom. The flexible modes can be avoided and the hydraulic 6-DOF parallel mechanism can still be considered as rigid by replacing the O-rings of the step-seals of the guide sleeve by ones with less elasticity, which is of great engineering significance to ensure the dynamic characteristics of the parallel mechanism.

Author Contributions: Conceptualization, C.Z.; methodology, C.Z.; software, C.Z.; validation, C.Z.; formal analysis, C.Z.; investigation, H.J.; resources, H.J.; data curation, C.Z.; writing—original draft preparation, C.Z.; writing—review and editing, H.J.; supervision, H.J. All authors have read and agreed to the published version of the manuscript.

Funding: This research received no external funding.

Institutional Review Board Statement: Not applicable.

Informed Consent Statement: Not applicable.

Conflicts of Interest: The authors declare no conflict of interest.

References

1. Huang, T.; Dong, C.L.; Liu, H.T.; Sun, T. A simple and visually orientated approach for type synthesis of overconstrained 1T2R parallel mechanisms. *Robotica* **2018**, *37*, 1161–1173. [CrossRef]
2. Chen, X.L.; Jiang, D.Y. Design, kinematics, and statics of a novel wave energy converter with parallel mechanism. *Int. J. Adv. Robot. Syst.* **2019**, *16*, 1729881419876214. [CrossRef]
3. Tian, W.J.; Shen, Z.Q.; Lv, D.P.; Yin, F.W. A Systematic Approach for Accuracy Design of Lower-Mobility Parallel Mechanism. *Robotica* **2020**, *38*, 2173–2188. [CrossRef]
4. Huang, T.; Dong, C.L.; Liu, H.T.; Zhang, J.X. Conceptual design and dimensional synthesis of a novel parallel mechanism for lower-limb rehabilitation. *Robotica* **2019**, *37*, 469–480.
5. Zhu, C.X.; Katupitiya, J.; Wang, J. Effect of links deformation on motion precision of parallel manipulator based on flexible dynamics. *Ind. Robot Int. J.* **2017**, *44*, 776–787. [CrossRef]
6. Gu, X.Y.; Li, C.S.; Xiao, X.; Lim, C.M.; Ren, H.L. A Compliant Transoral Surgical Robotic System Based on a Parallel Flexible Mechanism. *Ann. Biomed. Eng.* **2019**, *47*, 1329–1344. [CrossRef] [PubMed]
7. Liu, S.Z.; Dai, J.S.; Shen, G.; Li, A.M.; Cao, G.H.; Feng, S.Z.; Meng, D.Y. Dynamic analysis of spatial parallel manipulator with rigid and flexible couplings. *J. Cent. South Univ.* **2017**, *24*, 840–853. [CrossRef]
8. Chen, X.L.; Wu, L.K.; Deng, Y.; Wang, Q. Dynamic response analysis and chaos identification of 4-UPS-UPU flexible spatial parallel mechanism. *Nonlinear Dyn.* **2016**, *87*, 2311–2324. [CrossRef]
9. Firoozabadi, A.E.; Ebrahimi, S.; Amirian, G. Dynamic characteristics of a 3-RPR planar parallel manipulator with flexible intermediate links. *Robotica* **2015**, *33*, 1909. [CrossRef]

10. Wu, J.; Yu, G.; Gao, Y.; Wang, L.P. Mechatronics modeling and vibration analysis of a 2-DOF parallel manipulator in a 5-DOF hybrid machine tool. *Mech. Mach. Theory* **2018**, *121*, 430–445. [CrossRef]
11. Wang, S.T.; Cheng, G.; Chen, X.H.; Yang, J.H. Natural frequency analysis and experiment for 3SPS+1PS parallel hip joint manipulator based on rigid-flexible coupling theory. *J. Mech. Sci. Technol.* **2017**, *31*, 1447–1462. [CrossRef]
12. Yang, L.W.; Fang, Y.C.; Chai, F.M.; Dong, D.Y. Parameter Calibration of 6-Degree-of-Freedom Parallel Mechanism Based on Orthogonal Displacement Measuring System. *Optik* **2020**, *226*, 165806.
13. Gao, C.H.; Zheng, S.T.; Cong, D.C.; Han, J.W.; Yang, Z.D.; Sun, J.Y. Modeling and control of the cscec multi-function testing system. *J. Earthq. Eng.* **2018**, *2*, 257–280. [CrossRef]
14. Tao, H.; Qu, Z.Y.; Cong, D.C. Hybrid Position/Force Control Scheme for Hydraulic Parallel Manipulator. *Nongye Jixie Xuebao* **2018**, *49*, 361–366.
15. Zhang, L.P.; Cong, D.C.; Yang, Z.D.; Zhang, Y.Y.; Han, J.W. Robust tracking and synchronization of double shaking tables based on adaptive sliding mode control with novel reaching law. *IEEE Access* **2016**, *4*, 8686–8702. [CrossRef]
16. Gao, C.H.; Cong, D.C.; Liu, X.C.; Yang, Z.D.; Tao, H. Hybrid position/force control of 6-dof hydraulic parallel manipulator using force and vision. *Ind. Robot Int. J.* **2016**, *43*, 274–283. [CrossRef]
17. Jiang, H.Z.; He, J.F.; Tong, Z.Z. Modal space control for a hydraulically driven stewart platform. *J. Control Eng. Technol.* **2012**, *3*, 106–115.
18. Tian, T.X.; Jiang, H.Z.; Huang, Q.T.; He, J.F.; Nie, B.X. Control strategy of modal space for a hydraulically-driven stewart platform considering passive joint damping. *J. South China Univ. Technol. (Nat. Sci.)* **2015**, *43*, 56–62.
19. Li, R.Z. Analysis and Optimal Structure Design of A High-Frequency Band 6-Dof Parallel Manipulator. In Proceedings of the Dissertation for the Master Degree in Engineering, Harbin Institute of Technology, Harbin, China, June 2014.
20. Tomskis, L.; Uzny, S. A hydraulic cylinder subjected to Euler's load in aspect of the stability and free vibrations taking into account discrete elastic elements. *Arch. Civ. Mech. Eng.* **2011**, *11*, 769–785. [CrossRef]
21. Posiadala, B.; Cekus, D. Discrete model of vibration of truck crane telescopic boom with consideration of the hydraulic cylinder of crane radius change in the rotary plane. *Autom. Constr.* **2008**, *17*, 245–2508. [CrossRef]
22. Tian, T.X.; Jiang, H.Z.; Tong, Z.Z.; He, J.F.; Huang, Q.T. An inertial parameter identification method of eliminating system damping effect for a six-degree-of-freedom parallel manipulator. *Chin. J. Aeronaut.* **2015**, *28*, 582–592. [CrossRef]
23. Zhang, Q.; Mills, J.K.; Cleghornet, L.W.; Jin, J.M.; Zhao, C.S. Trajectory tracking and vibration suppression of a 3-PRR parallel manipulator with flexible links. *Multibody Syst. Dyn.* **2015**, *33*, 27–60. [CrossRef]